



Robust nickel single-atom catalyst for high-efficiency and stable vanadium-cerium redox flow batteries

Lei Wang^{1,2}, Weiming Chen^{2,*}, Han Qi^{2,3}, Cuizhu Ye⁴, Binglei Liu^{2,3}, Deliang Zeng^{2,3}, Zhuoyu Ji¹, Jia Hong Pan^{1,5,*}, Xiaolei Huang^{2,*}

Keywords:

Redox flow batteries, vanadium-cerium, redox reaction kinetics, single atom catalysts

Citation:

Wang, L.; Chen, W.; Qi, H.; Ye, C.; Liu, B.; Zeng, D.; Ji, Z.; Pan, J. H.; Huang, X. Robust nickel single-atom catalyst for high-efficiency and stable vanadium-cerium redox flow batteries. *Energy Mater.* 2026, 6, 600034. <https://dx.doi.org/10.20517/energymater.2025.223>

Received: 20 Dec 2025

First Decision: 9 Jan 2026

Revised: 2 Feb 2026

Accepted: 28 Feb 2026

Published: 8 Apr 2026

Academic Editor:

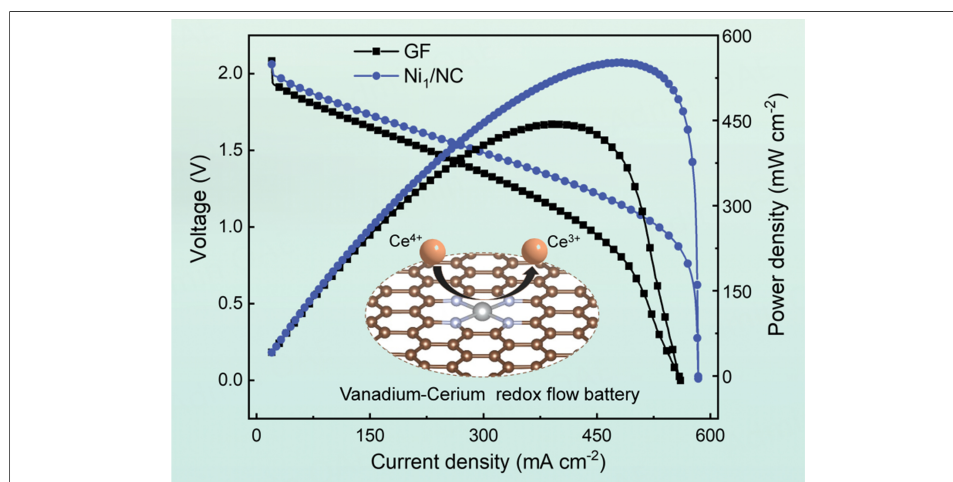
Yuhui Chen

Copy Editor:

Pei-Yun Wang

Production Editor:

Pei-Yun Wang



Abstract

Vanadium-cerium redox flow batteries (V-Ce RFBs) have emerged as a promising alternative to all-vanadium systems due to the lower cost and high standard redox potential of $\text{Ce}^{3+}/\text{Ce}^{4+}$. However, their practical application is hindered by the sluggish kinetics of the $\text{Ce}^{3+}/\text{Ce}^{4+}$ redox reaction and the severe corrosion of conventional graphite felt electrodes. To address these challenges, we constructed a single atomic nickel catalyst (Ni_1/NC) with a four-nitrogen coordination structure ($\text{Ni}_1\text{-N}_4$ moiety) on nitrogen-doped carbon support. The Ni_1/NC catalyst with high Ni loading possesses abundant accessible active sites and unique structure properties for catalysis. When applied as a positive electrode, the Ni_1/NC catalyst exhibited significantly enhanced electrocatalytic activity and stability for $\text{Ce}^{3+}/\text{Ce}^{4+}$ redox. The assembled V-Ce RFBs achieves a high energy efficiency of 69.1% at 200 mA cm^{-2} and a superior peak power density, markedly outperforming cells with baseline electrodes. Density functional theory calculations reveal that the $\text{Ni}_1\text{-N}_4$ sites

¹Collage of Environmental Science and Engineering, North China Electric Power University, Beijing 102206, China.

²Key Laboratory of Rare Earths, Ganjiang Innovation Academy, Chinese Academy of Sciences, Ganzhou 341000, Jiangxi, China.

³School of Rare Earths, University of Science and Technology of China, Hefei 230026, Anhui, China.

⁴School of Food Science and Engineering, South China University of Technology, Guangzhou 510640, Guangdong, China.

⁵International Joint Center of Nature-Inspired Carbon Neutrality Solutions, School of Resources, Environments and Materials, Guangxi University, Nanning 530004, Guangxi, China.

*Correspondence to: Prof. Xiaolei Huang, Dr. Weiming Chen, Key Laboratory of Rare Earths, Ganjiang Innovation Academy, Chinese Academy of Sciences, Ganzhou 341000, Jiangxi, China. E-mail: xluang@gia.cas.cn; wmchen@gia.cas.cn; Prof. Jia Hong Pan, International Joint Center of Nature-Inspired Carbon Neutrality Solutions, School of Resources, Environments and Materials, Guangxi University, Nanning 530004, Guangxi, China. E-mail: jhpan@gxu.edu.cn

facilitate charge transfer and enhance activation of reactant species (Ce^{4+}), providing atomic-level insight into the catalytic mechanism. This work demonstrates the effectiveness of single-atom catalysts in enhancing the performance of V-Ce RFBs and sheds light on designing advanced electrocatalysts.

INTRODUCTION

Amid the global transition toward low-carbon energy systems, the rapid expansion of solar and wind power has intensified the demand for advanced energy storage technologies capable of mitigating the intermittency and volatility inherent to these renewable sources^[1,2]. Redox flow batteries (RFBs), which store and release electrical energy via reversible redox reactions between the catholyte and anolyte, are widely regarded as one of the most promising technologies for large-scale energy storage applications due to their inherent safety and long cycle life^[3,4]. Within the landscape of RFBs technologies, all-vanadium systems (VRFBs) have emerged as a focal point of extensive research and development^[5-7]. However, the biological toxicity and high cost of vanadium compounds (e.g., V_2O_5 at $\approx \$10,200$ per ton) remain major obstacles, motivating the exploration for alternative redox couples^[8,9].

Recently, the $\text{Ce}^{3+}/\text{Ce}^{4+}$ redox couple has been demonstrated as a compelling candidate, owing to the significantly lower cost of cerium (the price of CeO_2 is around one-tenth that of V_2O_5) and the high standard redox potential of $\text{Ce}^{3+}/\text{Ce}^{4+}$ [1.72 V vs. standard hydrogen electrode (SHE)]^[10]. However, this strong oxidizing capability also accelerates electrode corrosion and degradation in acidic media, undermining system stability^[11]. Consequently, the practical implementation of vanadium-cerium (V-Ce) RFBs is largely constrained by the performance of the positive electrode^[12,13]. Owing to the strong acid electrolyte environment, electrodes based on metals and metal oxides are prone to dissolution. However, graphite felt (GF), the most commonly used electrode material in RFBs, offers limited intrinsic catalytic activity and insufficient stability during extended cycling^[14,15]. This limitation becomes more pronounced at elevated operating voltages, which accelerate electrode corrosion and lead to the formation of degradation products such as CO and CO_2 ^[16]. Additionally, the scarcity of available active sites on GF results in sluggish $\text{Ce}^{3+}/\text{Ce}^{4+}$ redox reaction kinetics, thereby constraining the energy efficiency (EE), discharge capacity, and power density of the system^[17]. Collectively, these issues significantly impair the overall charge-discharge performance of V-Ce RFBs.

Single-atom catalysts (SACs) have recently emerged as a highly promising class of electrocatalysts due to their maximum atom utilization, well-defined active sites, and unique electronic structures^[18,19]. Various SACs can be deposited and stabilized on various supports (e.g., carbon, oxide, metal, and zeolite), providing broad structural flexibility and catalytic feasibilities^[20,21]. Their abundant accessible active sites and unique coordination environments make SACs particularly attractive for enhancing electrocatalytic activity and stability in RFB systems^[22]. For VRFBs, SACs anchored on heteroatom-doped carbon substrates have demonstrated excellent resistance to strongly acidic electrolytes^[23]. For example, Xing *et al.* developed Bi SACs supported on GF that enabled a remarkable peak power density of 990 mW cm^{-2} at 240 mA cm^{-2} for VRFBs^[24]. However, existing research has focused almost exclusively on VRFBs, leaving their catalytic behavior and mechanistic roles in V-Ce RFBs largely unexplored^[25].

Herein, we constructed a nickel-based single atomic catalyst (Ni_1/NC) with a four-nitrogen coordination structure ($\text{Ni}_1\text{-N}_4$ moiety) on nitrogen-doped carbon (NC) support. The atomic dispersion and coordination environment of Ni SACs were confirmed by aberration correction high-angle annular dark-field scanning transmission electron microscopy (AC HAADF-STEM), X-ray absorption fine structure (XAFS), and density functional theory (DFT) calculation. Compared to pristine GF and NC, Ni_1/NC exhibited significantly enhanced electrocatalytic activity toward the $\text{Ce}^{3+}/\text{Ce}^{4+}$ redox reaction. When employed as the positive

electrode in a V-Ce RFB, the Ni_i/NC-modified electrode delivers a high EE of 65.1% at 200 mA cm⁻² over 100 cycles and a peak power density of 551.4 mW cm⁻², outperforming the NC-modified electrode (42.8% and 466.4 mW cm⁻²) and pristine GF (41.5% and 443.4 mW cm⁻²). DFT analysis further reveals that the Ni_i-N₄ moiety serves as the primary active center, enhancing charge transfer and reducing the reaction energy barrier at the electrode-electrolyte interface. This work demonstrates the effectiveness of SACs in V-Ce RFBs and provides valuable insights into the rational design of next-generation electrocatalysts for high-performance RFBs.

EXPERIMENTAL

Materials

All chemicals were purchased from commercial suppliers and used without further purification: VOSO₄ (Aladdin, shanghai, China); Ce₂(CO₃)₃ (Aladdin, shanghai, China); H₂SO₄ (XILONG SCIENCE, Guangdong, China); CH₄O₃S (Sigma-Aldrich, shanghai, China); NiCl₂·6H₂O (Aladdin, shanghai, China); Zn(NO₃)₂·6H₂O (Aladdin, shanghai, China); C₅H₈N₂ (Aladdin, shanghai, China); KCl (Aladdin, shanghai, China); Hydrochloric acid (Aladdin, shanghai, China); Ethanol (Aladdin, shanghai, China); Nafion D520 Dispersion (Chemours, shanghai, China); and C₃H₈O (Aladdin, shanghai, China).

Synthesis of NC, Ni_i/NC and Ni_{NP}/NC

NC support was firstly synthesized by updating the method in literature^[26]. Typically, 25.5 g Zn(NO₃)₂·6H₂O and 58.3 g 2-methylimidazole were dissolved separately in 2.0 L of deionized water. Then, the two solutions were mixed rapidly and stirred vigorously for 2 h. The resulting white suspension was aged under undisturbed conditions for 12 h to form a white precipitate. Next, the white precipitate was collected by filtration, and subsequently washed with water and ethanol to yield two-dimensional (2D) ZIF-8. Then, 10 g 2D ZIF-8 and 200 g KCl were dispersed in 800 mL deionized water and then dried by rotary evaporation to obtain a composite powder. The powder was pyrolyzed at 700 °C for 5 h under a continuous Ar flow with a controlled ramp rate of 2 °C·min⁻¹. The resultant solid was subjected to sequential washing cycles with 2 M HCl, deionized water, and ethanol, followed by an overnight dehydration process at 80 °C.

Then 500 mg of NC was dispersed in 50 mL of ethanol and sonicated for 30 min. Subsequently, 50 mL of ethanol containing 250 mg NiCl₂·6H₂O was added, and the mixture was magnetically stirred for an additional 2 h. After drying with a rotary evaporator, the mixture was transferred into a tube furnace and pyrolyzed at 300 °C for 5 h with a heating rate of 5 °C·min⁻¹ under an Ar flow. The yielded black powder was washed with an ethanol/water mixture several times and dried at 80 °C overnight. The resulting solid was pyrolyzed at 550 °C for 5 h with a heating rate of 2 °C·min⁻¹ under a flowing Ar atmosphere and yielded the Ni_i/NC catalyst.

For comparison, Ni nanoparticles loading on NC support (denoted as Ni_{NP}/NC) was synthesized using an identical procedure for Ni_i/NC but omitting the initial pyrolysis step at 300 °C.

Material characterization

Transmission electron microscopy (TEM) images, HAADF-STEM image, and energy-dispersive X-ray spectroscopy (EDS) were performed on JEM-2100F (JEOL, Tokyo, Japan) at 200 kV. AC HAADF-STEM images were performed on a JEOL JEM-ARM300F (JEOL, Tokyo, Japan) at 300 kV. X-ray diffraction (XRD) patterns were recorded on a D8 Advance (Bruker, Germany) diffractometer with Cu K α radiation (λ = 1.5418 Å) at 40 kV and 40 mA. X-ray photoelectron spectroscopy (XPS) measurement was performed on a Shimadzu AXIS SUPRA+ spectrometer (Shimadzu corporation, Japan) using Al K α radiation. Raman spectra were recorded with an in Via Raman spectrometer (Renishaw, UK) using 532 nm excitation at room temperature. N₂ adsorption and desorption isotherms were measured on a Micromeritics ASAP 2460

(Micromeritics instrument, USA) surface area and porosity analyzer at 77 K. The differential electrochemical mass spectrometry (DEMS) was measured on Shanghai Linglu QAS100-1 mass spectrometer (Shanghai Linglu, China). The XAFS spectra (Ni K-edge) were collected at the beamline BL13SSW station of the Shanghai Synchrotron Radiation Facility (SSRF). The acquired extended X-ray absorption fine structure (EXAFS) data were processed based on the standard procedures using the ATHENA module^[27].

Electrochemical measurement of Ni_i/NC, Ni_{NP}/NC, and NC catalysts

Ni_i/NC, Ni_{NP}/NC, and NC catalysts were deposited onto pristine GF substrates to fabricate the working electrodes. Specifically, 10 mg of catalyst was dispersed in a mixture containing 600 μ L of isopropanol, 150 μ L of ultrapure water, and 50 μ L of Nafion solution via ultrasonication. The resulting homogeneous ink was uniformly sprayed onto both sides of the GF using an airbrush, followed by drying. For comparative analysis, the prepared electrodes are denoted as Ni_i/NC, Ni_{NP}/NC, and NC electrodes.

The electrochemical tests were performed in a typical three-electrode cell. The working electrode is a 2 cm² GF, NC, and Ni_i/NC electrode, the counter electrode is titanium plate, and the reference is a saturated calomel electrode (SCE). The electrolyte consisted of 15 mL solution containing 0.05 M Ce₂(CO₃)₃, 3 M methanesulfonic acid (MSA), and 0.5 M H₂SO₄. Potentiostatic electrochemical impedance spectroscopy (PEIS) were collected with a CS3104 electrochemical workstation at an applied amplitude of 10 mV within the frequency range from 0.01 Hz to 1.0 M Hz.

RFB performance evaluation

In a typical RFB configuration, a Nafion N117 cation exchange membrane and electrodes (4 cm²) were compressed and sealed using two titanium end plates, with a rubber gasket serving as the sealing ring. During operation, the positive electrolyte consisted of 20 mL solution containing 0.2 mol·L⁻¹ Ce₂(CO₃)₃, 3 mol·L⁻¹ MSA, and 0.5 mol·L⁻¹ H₂SO₄, while the negative electrolyte comprised 8 mL solution containing 1 mol·L⁻¹ VOSO₄, 3 mol·L⁻¹ MSA, and 0.5 mol·L⁻¹ H₂SO₄. The positive electrode was composed of 2 × 2 cm² GF, NC, Ni_{NP}/NC, and Ni_i/NC, while the negative electrode was a GF of identical dimensions. The performance of V-Ce RFBs was characterized using a LANHE G340A charge-discharge testing system. The charge-discharge voltage window was controlled within the range of 0.6-2.2 V. Rate capability was evaluated through stepwise current density tests (40-200 mA cm⁻²), with each test condition subjected to five charge-discharge cycles to ensure data reliability. Additionally, the galvanostatic intermittent titration technique (GITT) was employed at 80 mA cm⁻² to analyze the kinetic characteristics of electrode reactions. These results provided critical insights into the catalytic activity, stability, and electrical conductivity of the electrode materials. All experiments were performed under strictly controlled environmental conditions to ensure the comparability and accuracy of the data.

Computational details

DFT calculations were performed using the Vienna Ab initio Simulation Package (VASP). The exchange-correlation interactions were treated within the generalized gradient approximation (GGA) using the Perdew-Burke-Ernzerhof (PBE) functional^[28,29]. The electron-ion interactions were modeled with the projector augmented wave (PAW) method, with a plane-wave basis set defined by a kinetic energy cutoff of 450 eV. For electronic structure iterations, a convergence criterion of 10⁻⁴ eV was established to ensure self-consistency. Additionally, the partial occupancies of the Kohn-Sham orbitals were refined using a Gaussian smearing width of 0.05 eV^[30]. Structural relaxations were performed until the maximum force on any atom was less than 0.05 eV·Å⁻¹. The formation energy (E_f) was evaluated according to the following expression^[31]:

$$E_f = E_{\text{tot}} - n_C \mu_C - n_{\text{Ni}} \mu_{\text{Ni}} - n_{\text{N}} \mu_{\text{N}} \quad (1)$$

Where E_{tot} denotes the total energy of the configured system; n_{C} , n_{Ni} , and n_{N} represent the number of carbon, nickel, and nitrogen atoms, respectively; and μ_{C} , μ_{Ni} , and μ_{N} refer to the chemical potentials of carbon, nickel, and nitrogen, referenced to graphite, hexagonal close-packed (hcp) Ni metal, and the N_2 molecule, respectively. A negative E_f value indicates thermodynamic stability relative to the constituent elements. Additionally, the charge density difference was computed as^[32]:

$$\Delta\rho = \rho_{\text{ad/sub}} - \rho_{\text{ad}} - \rho_{\text{sub}} \quad (2)$$

Here, $\rho_{\text{ad/sub}}$ corresponds to the total charge density of the optimized adsorbate-substrate complex, while ρ_{ad} and ρ_{sub} represent the charge densities of the isolated adsorbate and substrate, respectively, each frozen in the geometry adopted in the fully relaxed composite system.

RESULTS AND DISCUSSION

Characterization of Ni_i/NC

Ni_i/NC SAC was prepared via an impregnation-pyrolysis strategy, as illustrated in Figure 1A. The morphology and atomic-level structure features of NC and Ni_i/NC were resolved. TEM images [Supplementary Figure 1] reveal that NC exhibits a 2D ultrathin nanosheet structure, consistent with the 2D structure of ZIF-8 precursor [Supplementary Figure 2]. The absence of graphite lattice fringes in the high-resolution TEM image [Supplementary Figure 1C] suggested the amorphous carbon structure of NC, which was further confirmed by Raman spectroscopy [Supplementary Figure 3]. N_2 sorption plots show that NC exhibits a typical microporous structure with average pore size of 4.2 nm and a large Brunauer-Emmett-Teller (BET) surface area of 1,827 m² g⁻¹ [Supplementary Figure 4]. For Ni_i/NC, both TEM images [Figure 1B, Supplementary Figures 5 and 6] and low-magnification HAADF-STEM image [Figure 1C] reveal a similar morphology to that of NC, indicating the atomic dispersion of Ni species. The absence of Ni nanoparticles was also verified by XRD [Supplementary Figure 7]. AC HAADF-STEM images of Ni_i/NC [Figure 1D and E] reveal numerous isolated bright dots, ascribed to individual Ni atoms due to the atomic number (Z) contrast between Ni and lighter elements in the support^[33]. Besides, EDS mapping revealed a uniform distribution of Ni, C, and N across the substrate, with a Ni and N mass fraction of 9.2% and 15.2%, respectively [Supplementary Figure 8 and Supplementary Table 1]. The high N content provides abundant sites for the anchoring of Ni single atoms.

XPS was then performed to study the valence states of Ni_i/NC [Figure 2A and B, Supplementary Table 1]. The Ni 2p spectrum of Ni_i/NC [Figure 2A] displays characteristic peaks at binding energies of 855.6 eV for Ni 2p_{3/2} and 872.6 eV for Ni 2p_{1/2}, along with corresponding satellite peaks, suggesting the oxidation state of Ni (Ni^{δ+}) resulting from the Ni-support interactions^[34]. In the N 1s spectrum of Ni_i/NC [Figure 2B], besides pyridinic N (397.8 eV), pyrrolic N (399.6 eV), graphitic N (400.8 eV), and oxidized N (402.5 eV), a peak located at 398.5 eV corresponding to Ni–N bonding is also observed, indicating the existence of Ni–N coordination structure in Ni_i/NC.

The chemical states and coordination environment of Ni were further investigated by using synchrotron radiation based XAFS. As illustrated in the normalized Ni K-edge X-ray absorption near edge structure (XANES) spectra [Figure 2C], the absorption threshold of Ni_i/NC is positioned between those of the Ni foil and NiO references, indicating that the Ni species in Ni_i/NC possess an intermediate oxidation state between 0 and +2. The Ni K-edge XANES spectra [Figure 2C] reveal the position of the rising edge of Ni_i/NC is between that of Ni foil and NiO, indicating that the oxidation state of Ni in Ni_i/NC is between Ni⁰ and Ni²⁺. The unique electronic structure of Ni arises from coordination-induced charge transfer from Ni to N/C atoms. The Fourier transformed (FT)-EXAFS spectrum [Figure 2D] only displays a single prominent peak

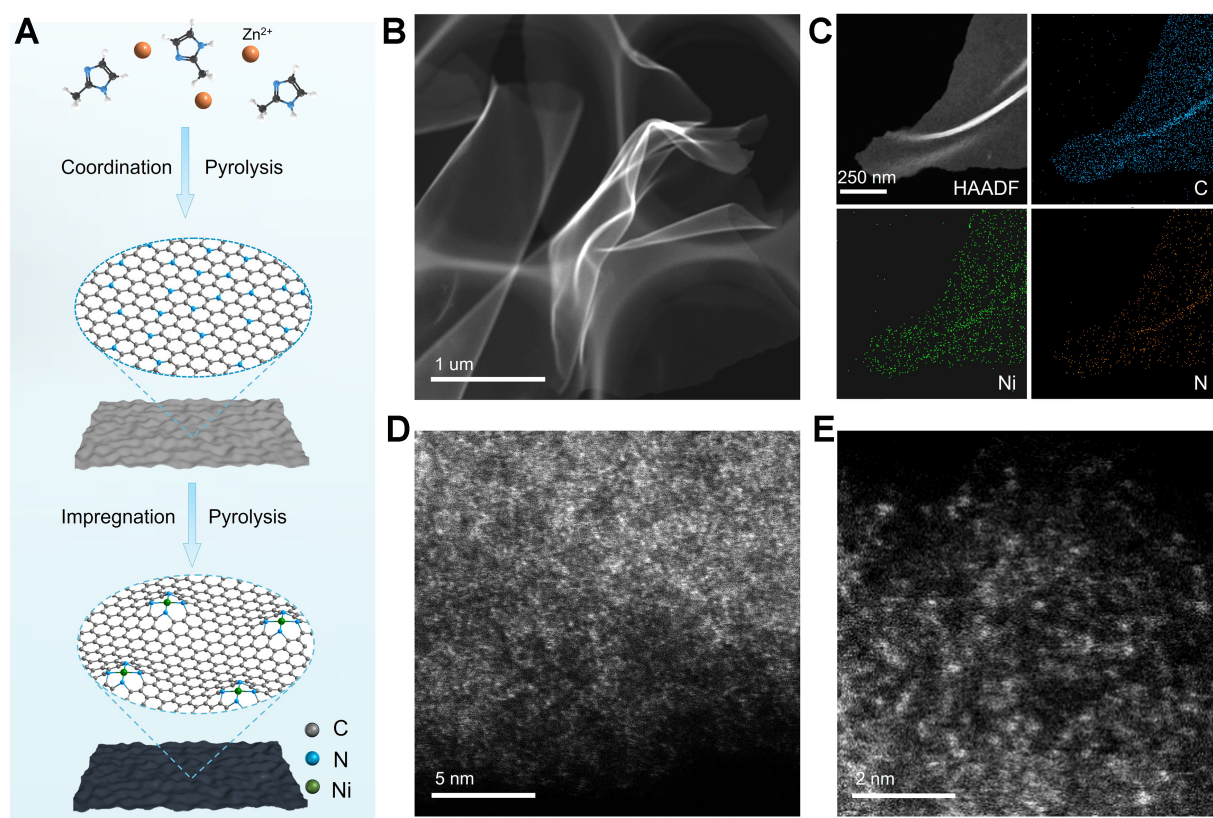


Figure 1. Synthesis process and structure characterizations of Ni₁/NC. (A) Schematic illustration of the synthesis process for Ni₁/NC; (B) Low-magnification HAADF-STEM image; (C) EDS element mapping, and (D and E) AC HAADF-STEM images of Ni₁/NC. NC: Nitrogen-doped carbon; HAADF-STEM: high-angle annular dark-field scanning transmission electron microscopy; EDS: energy-dispersive X-ray spectroscopy; AC: aberration correction.

(~ 1.5 Å), which is attributed to the Ni–N scattering, suggesting the atomically dispersed Ni species in Ni₁/NC^[35,36]. The k space of k^3 -weighted FT-EXAFS of Ni₁/NC [Supplementary Figure 9] reveals a unique profile that lacks the characteristic oscillations of Ni foil and NiO, further confirming the absence of nanoparticles. Wavelet transform (WT) analysis [Figure 2E] of Ni K -edge EXAFS oscillations only presents one maximum intensity (at ~ 4.5 Å^{−1}) which is assigned to the Ni–N coordination, further supporting the isolated nature of Ni atoms^[37]. Quantitative EXAFS curve fitting [Figure 2D and Supplementary Table 2] confirmed that the average Ni–N coordination number is estimated to be 3.8 with the average bond distance of 1.95 Å. Therefore, based on the EXAFS and XPS spectra, the local coordination structure of Ni in Ni₁/NC can be identified as Ni₁–N₄ (as displayed in the bottom of Figure 1A), where a single Ni atom is coordinated by four N atoms embedded within the carbon matrix.

Electrochemical performance for catalytic Ce³⁺/Ce⁴⁺ redox

Working electrodes were fabricated by depositing Ni₁/NC, or NC catalysts onto pristine GF substrates. The resulting electrodes were denoted as Ni₁/NC, NC, and GF (pristine graphite felt) electrodes for comparative purposes. The electrocatalytic activity and reaction kinetics of these electrodes toward the Ce⁴⁺/Ce³⁺ redox couple were evaluated in a standard three-electrode system. As shown in Figure 3A–C, well-defined oxidation and reduction peaks are observed in the cyclic voltammetry (CV) curves for all electrodes, suggesting appreciable reversibility of the Ce³⁺/Ce⁴⁺ redox reaction. A direct comparison of the CV curves acquired at 3 mV s^{−1} [Figure 3D] reveals that the NC and GF electrodes exhibit relatively low peak current densities and large peak potential separation (ΔE_p), indicating inferior electrocatalytic activity. In contrast, the Ni₁/NC electrode demonstrated significantly higher peak current densities ($I_{pa} = 31.1$ mA cm^{−2}, $I_{pc} =$

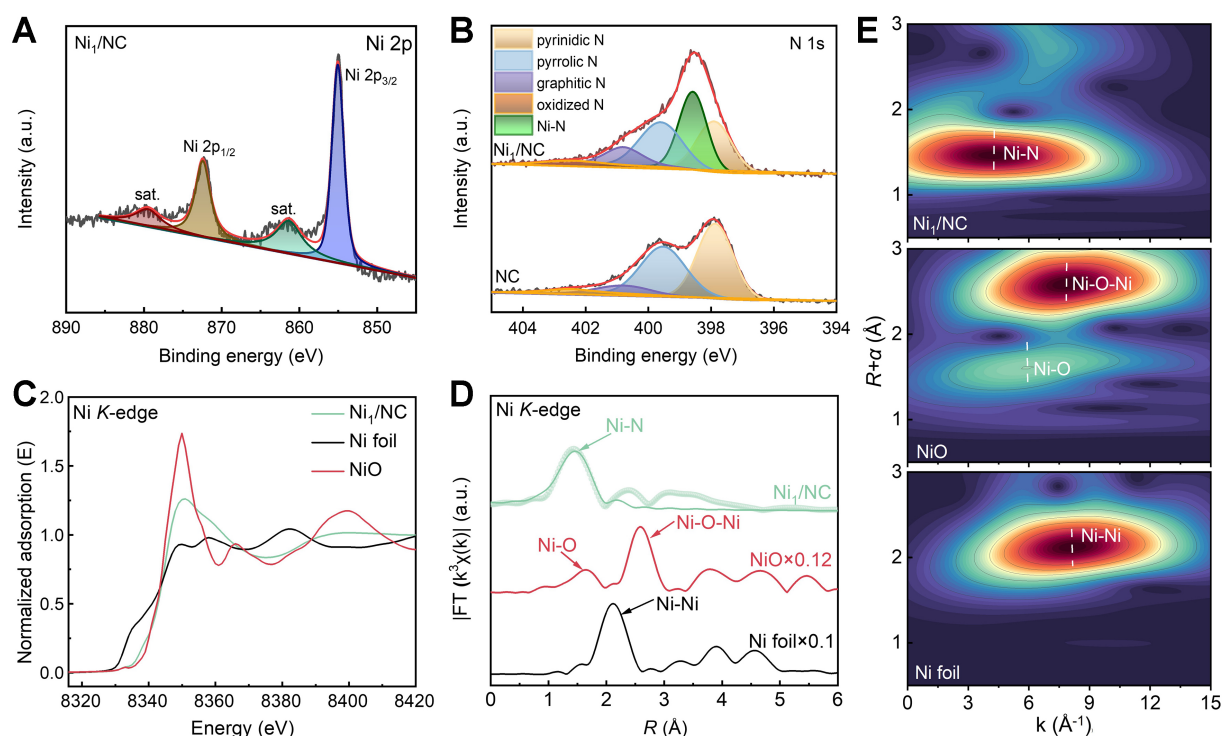


Figure 2. Chemical states and coordination environment of Ni₁/NC. (A) Ni 2p and (B) N 1s XPS spectra of samples; (C) Ni K-edge XANES, (D) FT-EXAFS, and (E) WT for the EXAFS signal of Ni₁/NC and references. NC: Nitrogen-doped carbon; XPS: X-ray photoelectron spectroscopy; XANES: X-ray absorption near edge structure; FT-EXAFS: Fourier transformed-extended X-ray absorption fine structure; WT: wavelet transform.

-24.5 mA cm⁻²) and a much smaller ΔE_p (0.46 V), indicating accelerated reaction kinetics and improved reversibility for the Ce⁴⁺/Ce³⁺ redox reaction. Additionally, as shown in Figure 3E, the peak current density (I_p) exhibits a highly linear relationship with the square root of the scan rate ($v_{1/2}$). For a reversible single-electron redox process, the peak current density is described by the Randles-Sevcik equation^[38]:

$$I_p = (2.69 \times 10^5) n^{3/2} A D_0^{1/2} C v^{1/2} \quad (3)$$

where I_p is in A cm⁻², $n = 1$, A (cm²) is the electroactive surface area, C (mol L⁻¹) is the bulk concentration of the redox mediator, D_0 (cm² s⁻¹) is the diffusion coefficient, and v (V s⁻¹) is the scan rate. The excellent linearity observed in the I_p vs. $v^{1/2}$ plots unambiguously confirms the diffusion-controlled nature of the redox process. Moreover, the steeper slope over Ni₁/NC electrode affords a higher apparent diffusion coefficient ($D_0 = 2.06 \times 10^{-3}$ cm² s⁻¹) than those over GF ($D_0 = 6.16 \times 10^{-4}$ cm² s⁻¹) and pristine NC ($D_0 = 1.02 \times 10^{-3}$ cm² s⁻¹), suggesting accelerated mass transport.

Figure 3F displays the Nyquist plots obtained from PEIS measurements for the Ni₁/NC, NC, and GF electrodes. The Ni₁/NC electrode exhibits a markedly lower charge transfer resistance ($R_{ct} = 3.7 \Omega$) compared to the NC (5.6 Ω) and GF (11.0 Ω) electrodes. The smaller R_{ct} value over the Ni₁/NC electrode is consistent with the decreased overpotential observed in the CV measurements, confirming that Ni₁/NC-modification significantly facilitates charge transfer kinetics. The nanostructured catalyst layer is also believed to increase the effective surface area of the electrode, thereby promoting ion diffusion^[39].

To confirm it, GITT measurements were conducted at 80 mA cm⁻², as shown in Figure 3G-I and

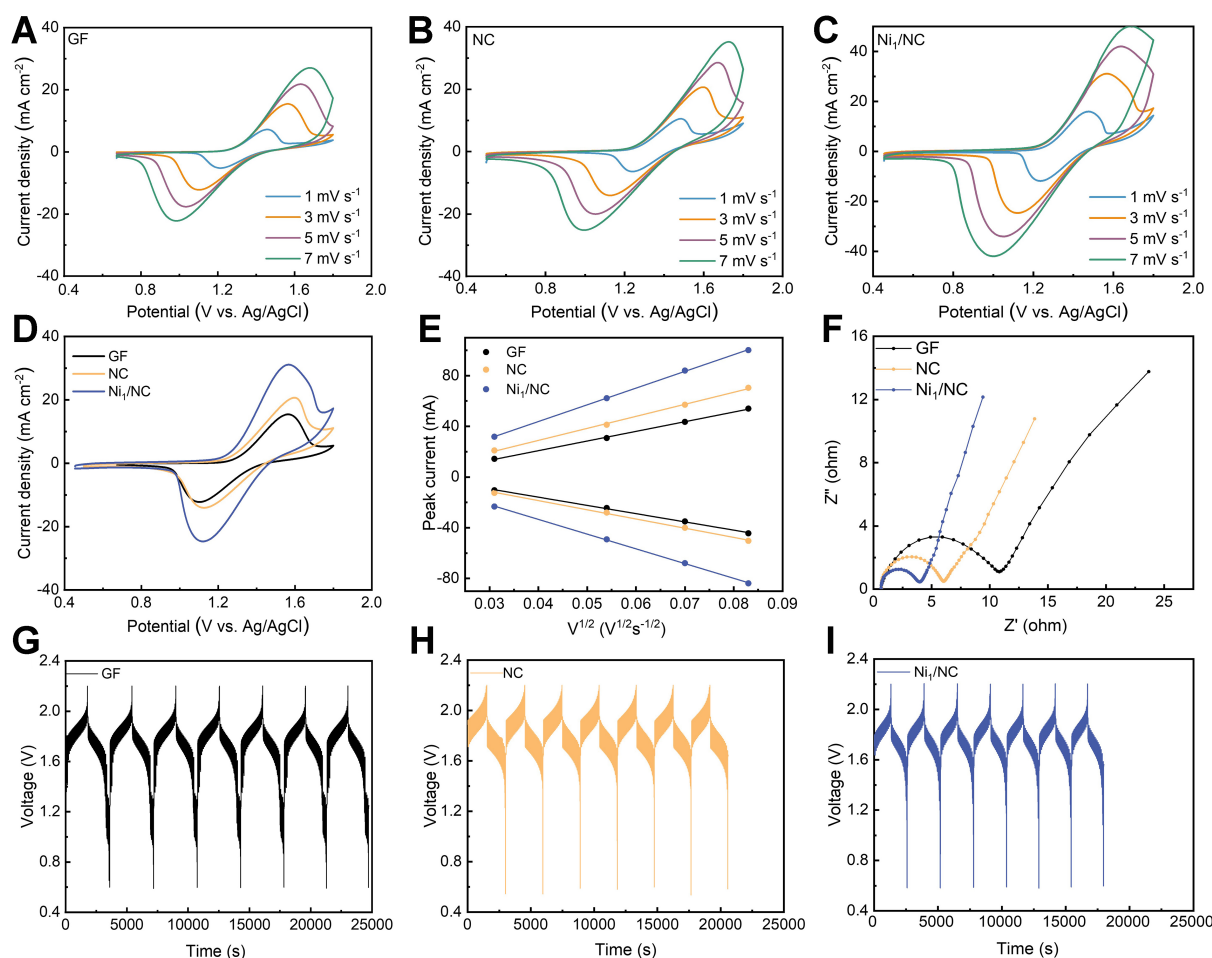


Figure 3. CV curves of (A) GF, (B) NC, and (C) Ni_I/NC; (D) CV curves of Ni_I/NC, NC, and GF at a scan rate of 3 mV s⁻¹; (E) Peak current density vs. the square root of scan rate derived from the CV curves in (D); (F) Nyquist plots of Ni_I/NC, NC, and GF (measured at open circuit potential); (G-I) Voltage profiles vs. time for the GF, NC, and Ni_I/NC electrodes at 80 mA cm⁻². CV: Cyclic voltammetry; GF: graphite felt; NC: nitrogen-doped carbon.

Supplementary Figure 10. The Ni_I/NC electrode exhibited smooth voltage changes and minimal polarization during the current pulses, indicating superior charge transfer properties. In contrast, the GF, NC, and its Ni nanoparticle counterpart (Ni_{NP}/NC) electrodes exhibited more pronounced voltage changes and polarization. The calculated ion diffusion coefficient (D) for Ni_I/NC (0.0035 cm² s⁻¹) was significantly higher than those for the NC (0.0020 cm² s⁻¹), GF (0.0016 cm² s⁻¹), and Ni_{NP}/NC (0.0017 cm² s⁻¹) electrodes, further confirming the enhanced ion transport kinetics within the Ni_I/NC-based electrode system.

RFB performance

To demonstrate the practical applicability of the catalysts, V-Ce redox flow cells were assembled using Ni_I/NC, NC, and GF as the positive electrode and pristine GF as the negative electrode. Energy efficiency (EE), defined as the product of coulombic efficiency (CE) and voltage efficiency (VE) ($EE = CE \times VE$), serves as a key indicator of energy conversion and storage capability during charge-discharge cycling^[40,41]. The rate performance of the flow cells is presented in Figure 4A and Supplementary Figure 11. As the current density increased from 40 to 200 mA cm⁻², the increasing overpotential and polarization caused a decreasing EE for all cells. Nevertheless, the cell with the Ni_I/NC electrode achieved a high EE of 69.1% at 200 mA cm⁻², significantly surpassing those of NC (53.8%), Ni_{NP}/NC (62.4%), and GF (47.3%). This superior performance primarily stems from the enhanced catalytic activity of the Ni_I/NC catalyst, which accelerates the reaction

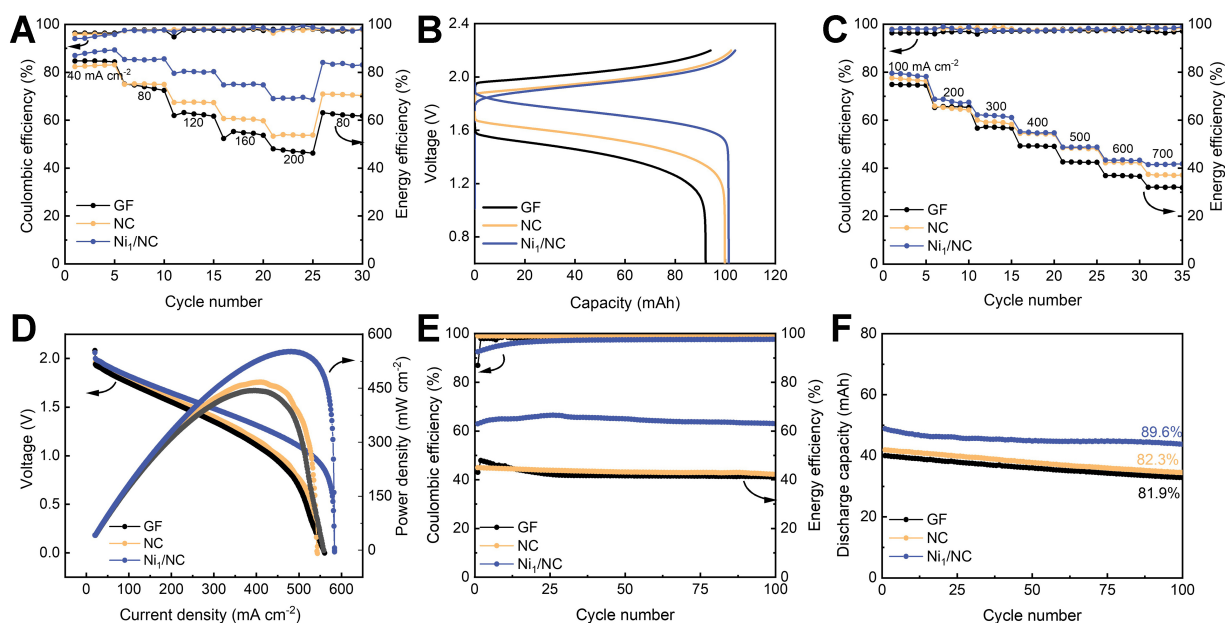


Figure 4. RFB performances. (A) Coulombic and energy efficiencies vs. cycle number of Ni_i/NC, NC, and GF at various current densities; (B) Voltage profiles vs. capacity of Ni_i/NC, NC, and GF at a current density of 80 mA cm⁻²; (C) CE and EE profiles of Ni_i/NC, NC, and GF charged at 80 mA cm⁻² and discharged under high current densities ranging from 100 to 700 mA cm⁻²; (D) Voltage and power density curves vs. current density of Ni_i/NC, NC, and GF; (E and F) Long-term cycling stability of Ni_i/NC, NC, and GF at 200 mA cm⁻². RFB: Redox flow battery; NC: nitrogen-doped carbon; GF: graphite felt; CE: coulombic efficiency; EE: energy efficiency.

kinetics and charge diffusion. When the current density was reduced from 200 to 80 mA cm⁻², the EE of the Ni_i/NC cell rapidly recovered to its previous level. The rapid recovery indicates lower polarization and higher inherent reversibility on the Ni_i/NC electrode^[42]. In contrast, cells with NC, Ni_{NP}/NC, and NC electrodes show limited recovery capability.

The charge-discharge profiles at 80 mA cm⁻² are presented in Figure 4B. Among the tested materials, Ni_i/NC exhibits the most favorable voltage characteristics - markedly lower charging potential, higher discharging potential, and significantly enhanced capacity. This improvement is directly attributable to the superior electrocatalytic activity of the Ni_i/NC electrode towards the Ce³⁺/Ce⁴⁺ redox reaction, which effectively reduces the reaction overpotential^[43,44]. Figure 4C displays the CE and EE of the three cells charged at 80 mA cm⁻² and discharged at current densities ranging from 100 to 700 mA cm⁻². During high-current-density discharge, the cell with Ni_i/NC electrode maintained a stable CE and demonstrated significantly superior energy efficiency retention across the entire range of discharge current densities compared to the other cells. Polarization curves shown in Figure 4D also reveal that the cell with the Ni_i/NC electrode reaches a higher peak power density (551.4 mW cm⁻²) than cells with NC (466.4 mW cm⁻²), Ni_{NP}/NC (475.8 mW cm⁻²), and GF (443.4 mW cm⁻²) electrodes. Furthermore, the cell with Ni_i/NC electrode sustains higher operating voltages across the entire current density range, suggesting its enhanced overall cell performance. These improvements are primarily due to the exceptional catalytic activity of Ni_i/NC, which reduces both charge transfer resistance and mass transfer resistance, thereby minimizing overpotential and endowing the cell outstanding electrochemical characteristics.

Long-term cycling stability was then evaluated by subjecting it to cycling 100 times at 200 mA cm⁻² [Figure 4E and F]. The cell with Ni_i/NC electrode maintains a high EE (65.1%) throughout the cycling test, demonstrating its satisfactory stability. Moreover, it also delivers a high capacity of 48.8 mAh and a remarkable capacity retention rate of 89.6% after 100 cycles, significantly superior to that of cells with NC

(41.8 mAh, 82.3% retention), Ni_{NP}/NC (44.5 mAh, 80.8% retention), and GF (40.0 mAh, 81.9% retention) electrodes. The excellent durability of cell with Ni_I/NC electrode stems from the chemical stability of Ni_I/NC catalyst in high current densities and strong acidic conditions, effectively mitigating the degradation processes of the cell. Moreover, the battery with Ni_I/NC electrodes also exhibited superior battery performance to those reported in most literature [Supplementary Table 3].

To further verify the structural and chemical robustness of the Ni_I/NC catalyst, comprehensive post-cycling characterizations were performed. SEM images [Supplementary Figure 12] show that the Ni_I/NC coating adheres firmly to the GF after long-term cycling. TEM and HAADF-STEM images [Supplementary Figure 13A and B] reveal there are no noticeable structural collapse or metal aggregation on Ni_I/NC catalyst. EDS mapping [Supplementary Figure 13C] demonstrates a uniform distribution of Ni and N elements and the Ni loading is similar to that of fresh catalysts. Further inductively coupled plasma optical emission spectroscopy (ICP-OES) analysis [Supplementary Table 4] also confirmed that the loss rate of Ni in Ni_I/NC catalyst was only 0.71 wt% after long-term cycling. XPS analysis [Supplementary Figure 14] further corroborates the chemical stability, despite the interference from F KLL Auger peaks (from the Nafion binder in preparing electrode), the core Ni-N coordination environment is well-preserved, as evidenced by the stable Ni 2p_{3/2} position and the persistent Ni-N_x signature in the N 1s spectrum. Moreover, online DEMS was employed to monitor gas evolution during operation [Supplementary Figure 15]. Compared to the pristine GF, the Ni_I/NC electrode exhibits significantly suppressed CO₂ evolution, indicating that the Ni_I/NC catalyst effectively mitigates carbon corrosion at high oxidative potentials. These results collectively demonstrate the exceptional morphological and chemical integrity of the Ni_I/NC catalyst, ensuring its long-term reliability in V-Ce RFBs.

Theoretical calculation analysis

DFT calculations were performed to unravel the origin of the exceptional electrocatalytic activity of Ni_I/NC toward the Ce³⁺/Ce⁴⁺ redox couple. The Ni-N₄ structural model [Figure 5A] was constructed based on the experimentally determined coordination number (3.8) and bond distance (1.95 Å) from EXAFS fitting. The thermodynamic stability of this moiety was subsequently confirmed by a calculated formation energy of -1.27 eV [Supplementary Figure 16]. Differential charge density analysis reveals pronounced electron depletion at the Ni center, and Bader charge quantification [Supplementary Table 5] indicates a transfer of 1.03 e⁻ from Ni to the N-doped carbon framework, and imparting strong Lewis acidity to the Ni site, thereby promoting the adsorption of Ce³⁺/Ce⁴⁺ species^[45]. Figure 5B illustrates the dehydration process of [Ce(H₂O)₉]³⁺, in which the strongly Lewis-acidic Ni atom effectively competes with water and weakens the Ce-OH₂ bonds, disrupts the original stable nine-coordinate structure of Ce³⁺, and exposes the metal center for direct electron transfer, thus endowing the Ni-N₄ site with excellent oxidative activity^[46,47].

The projected density of states [Figure 5C] reveals that the out-of-plane 3d_{z²} orbital of Ni dominates with a sharp peak straddling the Fermi level, accompanied by substantial unoccupied states. In contrast, the in-plane d-orbitals are deeply occupied, forming a highly anisotropic electronic structure which is conducive to axial interaction with Ce species^[48]. Meanwhile, the total density of states [Figure 5D] displays a symmetric spin distribution, indicating a non-magnetic ground state for the Ni_I/NC system. Despite the lack of net spin polarization, the Ni 3d orbitals exhibit significant hybridization with N-derived states near the Fermi level, creating a coordinatively unsaturated and electronically active environment. Notably, the states near the Fermi level are predominantly contributed by the Ni center and span a broad energy range, reflecting strong Ni-N coupling and high electron delocalization that effectively accelerate bidirectional electron transfer^[49]. Collectively, these electronic and structural features account for the excellent electrocatalytic activity of the Ni_I/NC catalyst.

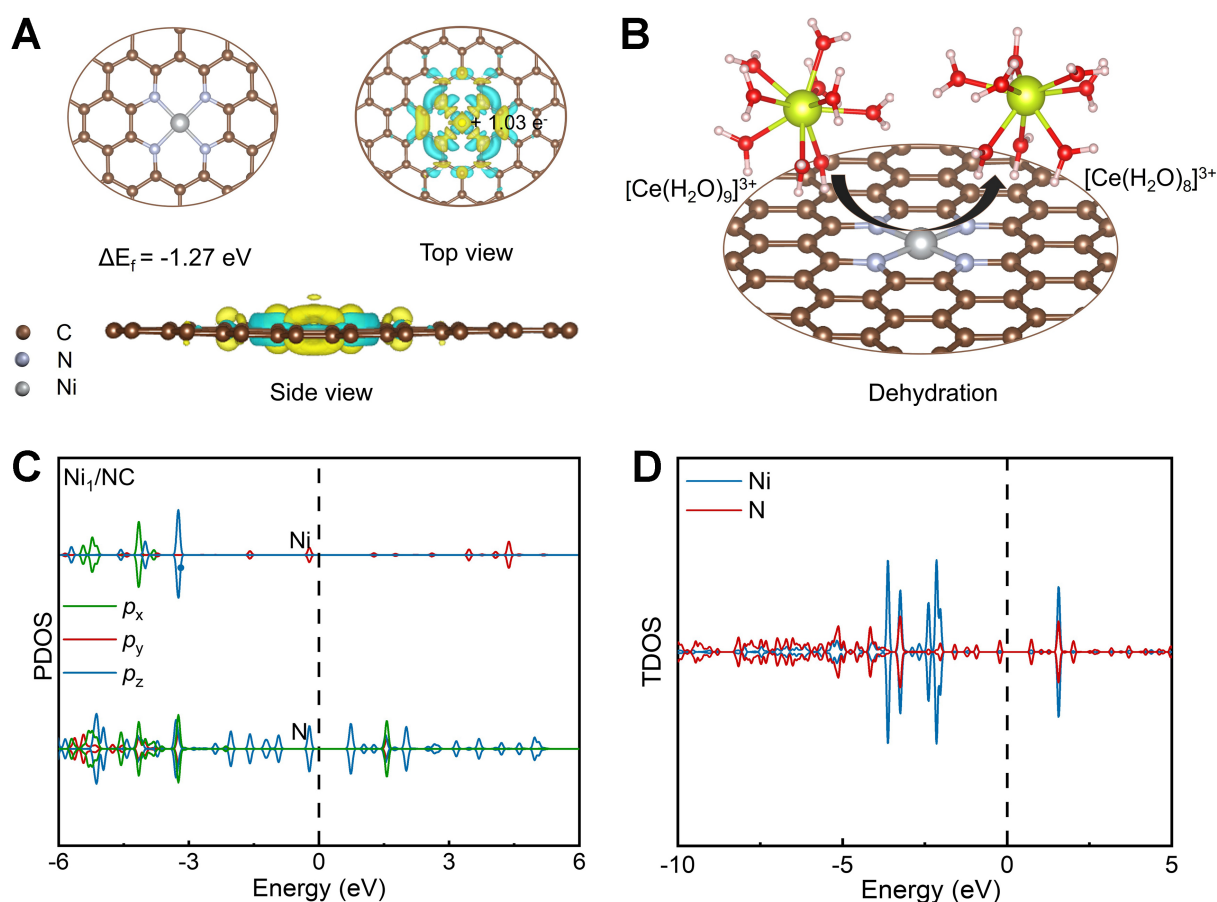


Figure 5. Theoretical calculations of Ni₁/NC. (A) Optimized Ni-N₄ configuration (the formation energy is -1.24 eV) and differential charge analysis of Ni₁/NC. The yellow and cyan iso-surfaces represent areas of electron enrichment and deficiency, respectively; (B) Schematic of the dehydration process from [Ce(H₂O)₉]³⁺ to [Ce(H₂O)₈]³⁺; (C) PDOS and (D) TDOS of Ni₁/NC. NC: Nitrogen-doped carbon; PDOS: projected density of states; TDOS: total density of states.

CONCLUSIONS

A single atomic Ni catalyst with a Ni₁-N₄ moiety on NC support has been successfully synthesized and used as advanced positive electrodes for high-performance V-Ce RFBs. Owing to the abundant accessible active sites and unique structural properties of Ni₁/NC for catalysis, Ni₁/NC-modified electrode exhibited significantly enhanced kinetics for the Ce³⁺/Ce⁴⁺ redox reaction and significantly improved overall performance for practical V-Ce RFBs compared to NC-modified and pristine GF electrodes. These improvements are attributed to the unique electronic structure of the Ni₁-N₄ sites, which facilitate charge transfer and enhance activation of reactant species (Ce⁴⁺), as elucidated by DFT calculations. This work demonstrates the effectiveness of SACs in enhancing the performance of V-Ce RFBs and sheds light on the design of advanced electrocatalysts.

DECLARATIONS

Acknowledgments

The authors acknowledge the financial supports from the Natural Science Foundation of Jiangxi, China (20232ACB203002) and the National Natural Science Foundation of China (22502210). The authors also thank Dr. Jianrong Zeng and the BL13SSW beamline at the Shanghai Synchrotron Radiation Facility (<https://cstr.cn/31124.02.SSRF.BL13SSW>) for the XAFS experiments supports.

Authors' contributions

Conceptualization, investigation, and writing: Wang, L.; Qi, H.; Ye, C.; Liu, B.; Zeng, D.; Ji, Z.; Huang, X.;

Chen, W.; Pan, J. H.

Supervision: Huang, X.; Chen, W.; Pan, J. H.

Availability of data and materials

The original contributions presented in this study are included in the article/[Supplementary Materials](#). Further inquiries can be directed to the corresponding authors.

AI and AI-assisted tools statement

During the preparation of this manuscript, the AI tool DeepSeek-R1 (version 1.0, released 2025-01-20) was used solely for language editing. The tool did not influence the study design, data collection, analysis, interpretation, or the scientific content of the work. All authors take full responsibility for the accuracy, integrity, and final content of the manuscript.

Financial support and sponsorship

This work was supported by the Natural Science Foundation of Jiangxi, China (20232ACB203002) and the National Natural Science Foundation of China (22502210 and 22461142141).

Conflicts of interest

All authors declared that there are no conflicts of interest.

Ethical approval and consent to participate

Not applicable.

Consent for publication

Not applicable.

Copyright

© The Author(s) 2026.

Supplementary Materials

[Supplementary Materials](#)

REFERENCES

1. Chu, S.; Cui, Y.; Liu, N. The path towards sustainable energy. *Nat. Mater.* **2016**, *16*, 16-22. [DOI PubMed](#)
2. Armstrong, R. C.; Wolfram, C.; de Jong, K. P.; et al. The frontiers of energy. *Nat. Energy.* **2016**, *1*, 15020. [DOI](#)
3. Noack, J.; Roznyatovskaya, N.; Herr, T.; Fischer, P. The chemistry of redox-flow batteries. *Angew. Chem. Int. Ed. Engl.* **2015**, *54*, 9776-809. [DOI PubMed](#)
4. Liu, Y.; Niu, Y.; Ouyang, X.; et al. Progress of organic, inorganic redox flow battery and mechanism of electrode reaction. *Nano. Res. Energy.* **2023**, *2*, e9120081. [DOI](#)
5. Jiang, H.; Sun, J.; Wei, L.; Wu, M.; Shyy, W.; Zhao, T. A high power density and long cycle life vanadium redox flow battery. *Energy. Storage. Mater.* **2020**, *24*, 529-40. [DOI](#)
6. Ye, L.; Qi, S.; Cheng, T.; et al. Vanadium redox flow battery: review and perspective of 3D electrodes. *ACS. Nano.* **2024**, *18*, 18852-69. [DOI PubMed](#)
7. Huang, Z.; Mu, A.; Wu, L.; Yang, B.; Qian, Y.; Wang, J. Comprehensive analysis of critical issues in all-vanadium redox flow battery. *ACS. Sustain. Chem. Eng.* **2022**, *10*, 7786-810. [DOI](#)
8. Lourenssen, K.; Williams, J.; Ahmadvour, F.; Clemmer, R.; Tasnim, S. Vanadium redox flow batteries: a comprehensive review. *J. Energy. Storage.* **2019**, *25*, 100844. [DOI](#)
9. Ulaganathan, M.; Aravindan, V.; Yan, Q.; Madhavi, S.; Skyllas-Kazacos, M.; Lim, T. M. Recent advancements in all-vanadium redox flow batteries. *Adv. Mater. Inter.* **2016**, *3*, 1500309. [DOI](#)
10. Wu, Y.; Zhou, L.; Xie, Y.; et al. A green europium-cerium redox flow battery with ultrahigh voltage and high performance. *Chem. Eng. J.* **2024**, *500*, 157189. [DOI](#)
11. Jelinek, L.; Wei, Y.; Mikio, K. Electro-oxidation of concentrated Ce(III) at carbon felt anode in nitric acid media. *J. Rare. Earths.* **2006**, *24*, 257-63. [DOI](#)

-
12. Zhang, X.; Liu, L.; Zhang, K.; et al. Modulating single-atom sulfur-vacancy defect in MoS_{2-x} catalysts to boost cathode redox kinetics for vanadium flow batteries. *Energy. Storage. Mater.* **2024**, *69*, 103442. DOI
 13. Hosseini, M. G.; Mousavihashemi, S.; Murcia-López, S.; Flox, C.; Andreu, T.; Morante, J. R. High-power positive electrode based on synergistic effect of N- and WO₃-decorated carbon felt for vanadium redox flow batteries. *Carbon* **2018**, *136*, 444-53. DOI
 14. Xing, F.; Liu, T.; Yin, Y.; et al. Highly active hollow porous carbon spheres@graphite felt composite electrode for high power density vanadium flow batteries. *Adv. Funct. Mater.* **2022**, *32*, 2111267. DOI
 15. Jiang, Y.; Wang, Y.; Cheng, G.; et al. Multiple-dimensioned defect engineering for graphite felt electrode of vanadium redox flow battery. *Carbon. Energy.* **2024**, *6*, e537. DOI
 16. Gong, W.; Yuan, Q.; Chen, C.; et al. Liberating N-CNTs confined highly dispersed Co–N_x sites for selective hydrogenation of quinolines. *Adv. Mater.* **2019**, *31*, e1906051. DOI PubMed
 17. Na, Z.; Wang, X.; Liu, X.; Li, W.; Sun, X. O/N/S trifunctional doping on graphite felts: a novel strategy toward performance boosting of cerium-based redox flow batteries. *Carbon. Energy.* **2021**, *3*, 752-61. DOI
 18. Qiao, B.; Wang, A.; Yang, X.; et al. Single-atom catalysis of CO oxidation using Pt₁/FeO_x. *Nat. Chem.* **2011**, *3*, 634-41. DOI
 19. Kaiser, S. K.; Chen, Z.; Faust Akl, D.; Mitchell, S.; Pérez-Ramírez, J. Single-atom catalysts across the periodic table. *Chem. Rev.* **2020**, *120*, 11703-809. DOI PubMed
 20. Yang, X. F.; Wang, A.; Qiao, B.; Li, J.; Liu, J.; Zhang, T. Single-atom catalysts: a new frontier in heterogeneous catalysis. *Acc. Chem. Res.* **2013**, *46*, 1740-8. DOI PubMed
 21. Wang, A.; Li, J.; Zhang, T. Heterogeneous single-atom catalysis. *Nat. Rev. Chem.* **2018**, *2*, 65-81. DOI
 22. Xing, F.; Wang, S.; Fu, Q.; Liu, T.; Li, X. Heteroatom-tuned Bi pz-orbital hybridization of single-atom catalysts for high-power density vanadium flow batteries. *Energy. Storage. Mater.* **2025**, *81*, 104472. DOI
 23. Wang, Z.; Lu, G.; Wei, T.; et al. Synergy of single atoms and sulfur vacancies for advanced polysulfide-iodide redox flow battery. *Nat. Commun.* **2025**, *16*, 2885. DOI PubMed PMC
 24. Xing, F.; Fu, Q.; Xing, F.; et al. Bismuth single atoms regulated graphite felt electrode boosting high power density vanadium flow batteries. *J. Am. Chem. Soc.* **2024**, *146*, 26024-33. DOI PubMed
 25. Huang, J.; He, G.; Huang, K.; et al. Atomic iron on porous graphene films for catalyzing the VO²⁺/VO₂⁺ redox couple in vanadium redox flow batteries. *Mater. Today. Phys.* **2023**, *35*, 101117. DOI
 26. Hai, X.; Xi, S.; Mitchell, S.; et al. Scalable two-step annealing method for preparing ultra-high-density single-atom catalyst libraries. *Nat. Nanotechnol.* **2022**, *17*, 174-81. DOI PubMed
 27. Chen, W.; Jin, H.; He, F.; Cui, P.; Cao, C.; Song, W. Dynamic evolution of nitrogen and oxygen dual-coordinated single atomic copper catalyst during partial oxidation of benzene to phenol. *Nano. Res.* **2022**, *15*, 3017-25. DOI
 28. Grimme, S.; Ehrlich, S.; Goerigk, L. Effect of the damping function in dispersion corrected density functional theory. *J. Comput. Chem.* **2011**, *32*, 1456-65. DOI PubMed
 29. Perdew, J. P.; Burke, K.; Ernzerhof, M. Generalized gradient approximation made simple. *Phys. Rev. Lett.* **1996**, *77*, 3865-8. DOI PubMed
 30. Kresse, G.; Joubert, D. From ultrasoft pseudopotentials to the projector augmented-wave method. *Phys. Rev. B.* **1999**, *59*, 1758-75. DOI
 31. Freysoldt, C.; Grabowski, B.; Hickel, T.; et al. First-principles calculations for point defects in solids. *Rev. Mod. Phys.* **2014**, *86*, 253-305. DOI
 32. Kresse, G.; Furthmüller, J. Efficient iterative schemes for ab initio total-energy calculations using a plane-wave basis set. *Phys. Rev. B. Condens. Matter.* **1996**, *54*, 11169-86. DOI PubMed
 33. Gawande, M. B.; Fornasiero, P.; Zbořil, R. Carbon-based single-atom catalysts for advanced applications. *ACS. Catal.* **2020**, *10*, 2231-59. DOI
 34. Santhosh Kumar, R.; Vijayapradeep, S.; Sakthivel, V.; Sayfiddinov, D.; Kim, A. R.; Yoo, D. J. Foam-like porous structured trimetal electrocatalysts exhibiting superior performance for overall water splitting and solid-liquid zinc-air batteries. *ACS. Appl. Mater. Interfaces.* **2025**, *17*, 10556-69. DOI PubMed
 35. Kumar, R. S.; Mannu, P.; Prabhakaran, S.; et al. Trimetallic oxide electrocatalyst for enhanced redox activity in zinc-air batteries evaluated by in situ analysis. *Adv. Sci.* **2023**, *10*, e2303525. DOI PubMed PMC
 36. Chen, W.; Che, Y.; Xia, J.; et al. Metal-sulfur interfaces as the primary active sites for catalytic hydrogenations. *J. Am. Chem. Soc.* **2024**, *146*, 11542-52. DOI PubMed
 37. Wu, J.; Cao, X.; Ji, Y.; et al. Boosting kinetics of Ce³⁺/Ce⁴⁺ redox reaction by constructing TiC/TiO₂ heterojunction for cerium-based flow batteries. *Adv. Funct. Mater.* **2024**, *34*, 2309825. DOI
 38. Deng, Q.; Huangyang, X.; Zhang, X.; et al. Edge-rich multidimensional frame carbon as High-Performance Electrode Material For Vanadium Redox Flow Batteries. *Adv. Energy. Mater.* **2022**, *12*, 2103186. DOI

39. Yuan, Z.; Liu, X.; Xu, W.; Duan, Y.; Zhang, H.; Li, X. Negatively charged nanoporous membrane for a dendrite-free alkaline zinc-based flow battery with long cycle life. *Nat. Commun.* **2018**, *9*, 3731. DOI PubMed PMC
40. Park, M.; Ryu, J.; Wang, W.; Cho, J. Material design and engineering of next-generation flow-battery technologies. *Nat. Rev. Mater.* **2017**, *2*, 16080. DOI
41. Zhang, L.; Jia, Y.; Liu, H.; et al. Charge polarization from atomic metals on adjacent graphitic layers for enhancing the hydrogen evolution reaction. *Angew. Chem. Int. Ed. Engl.* **2019**, *58*, 9404-8. DOI PubMed
42. Jiang, Y.; Liu, Z.; Lv, Y.; et al. Perovskite enables high performance vanadium redox flow battery. *Chem. Eng. J.* **2022**, *443*, 136341. DOI
43. Li, B.; Nie, Z.; Vijayakumar, M.; et al. Ambipolar zinc-polyiodide electrolyte for a high-energy density aqueous redox flow battery. *Nat. Commun.* **2015**, *6*, 6303. DOI PubMed PMC
44. Zhang, X.; Valencia, A.; Li, W.; et al. Decoupling activation and transport by electron-regulated atomic-Bi harnessed surface-to-pore interface for vanadium redox flow battery. *Adv. Mater.* **2024**, *36*, e2305415. DOI PubMed
45. Guo, J.; Pan, L.; Sun, J.; et al. Metal-free fabrication of nitrogen-doped vertical graphene on graphite felt electrodes with enhanced reaction kinetics and mass transport for high-performance redox flow batteries. *Adv. Energy. Mater.* **2024**, *14*, 2302521. DOI
46. Koppe, J.; Yakimov, A. V.; Gioffrè, D.; et al. Coordination environments of Pt single-atom catalysts from NMR signatures. *Nature* **2025**, *642*, 613-9. DOI PubMed PMC
47. Liu, Z.; Sun, Y.; Wang, Y.; et al. Optimal solution for modeling electrocatalysis on two-dimensional single-atom catalysts with grand canonical DFT. *ACS. Catal.* **2025**, *15*, 7993-8004. DOI
48. Zhao, X.; Wang, F.; Kong, X. P.; Fang, R.; Li, Y. Dual-metal hetero-single-atoms with different coordination for efficient synergistic catalysis. *J. Am. Chem. Soc.* **2021**, *143*, 16068-77. DOI PubMed
49. Yang, J.; Liu, W.; Xu, M.; et al. Dynamic behavior of single-atom catalysts in electrocatalysis: identification of Cu-N₃ as an active site for the oxygen reduction reaction. *J. Am. Chem. Soc.* **2021**, *143*, 14530-9. DOI PubMed

Disclaimer/Publisher's Note: All statements, opinions, and data contained in this publication are solely those of the individual author(s) and contributor(s) and do not necessarily reflect those of OAE and/or the editor(s). OAE and/or the editor(s) disclaim any responsibility for harm to persons or property resulting from the use of any ideas, methods, instructions, or products mentioned in the content.



© The Author(s) 2026. Open Access This article is licensed under a Creative Commons Attribution 4.0 International License (<https://creativecommons.org/licenses/by/4.0/>), which permits unrestricted use, sharing, adaptation, distribution and reproduction in any medium or format, for any purpose, even commercially, as long as you give appropriate credit to the original author(s) and the source, provide a link to the Creative Commons license, and indicate if changes were made.